RSC Advances

PAPER

View Article Online
View Journal | View Issue

Cite this: *RSC Adv.*, 2026, **16**, 11023

Single-beam femtosecond Z-scan studies of bismuth and manganese co-doped titanium dioxide nanoparticles dispersed in ethanol

G Krishna Podagatlapalli, *[a] Twinkle Jena,[a] Suresh Maddila,[b] Syed Hamad,[c] Saikiran Vadavalli,[a] Chandrasekhar Angani [a] and Venugopal Rao Soma[d]

We report the femtosecond (fs) nonlinear optical (NLO) properties of simultaneously co-doped bismuth (Bi) and manganese (Mn) in titanium dioxide (TiO_2) colloidal nanoparticles (NPs) dispersed in ethanol using ultrashort pulses of ~150 femtoseconds (fs) duration at an input wavelength of ~800 nm. The Bi and Mn co-doped TiO_2 NPs were prepared by a deposition and precipitation method. The enhancement of the photoresponse of TiO_2 (and the corresponding NPs) through metal doping has indeed become a promising area of research as it holds the potential to extend their applications in solar cells (as essential components), catalysis, and phototherapy. The band gap (3.2 eV) of the anatase crystalline phase of TiO_2 NPs was reduced to 3.0 eV, 2.7 eV, and 2.5 eV upon co-doping with Bi–Mn at Bi concentrations of 2.5%, 5%, and 10%, respectively. The co-doping of Bi and Mn in TiO_2 NPs significantly altered their band structure, enhancing their optical, mechanical, and chemical properties. A single beam Z-scan experiment was performed on Bi–Mn co-doped TiO_2 NP colloids in ethanol exposed to 150 fs pulses, at 800 nm central wavelength. The open aperture (OA) Z-scan traces of Bi–Mn co-doped TiO_2 NPs were obtained at a constant input power. The obtained NLO results demonstrated reverse saturable absorption (RSA) within saturable absorption (SA) and SA in RSA. The closed aperture (CA) Z-scan was also performed at 800 nm, displaying a negative value of the refractive index (intensity-dependent), which represents the self-defocusing effect. The typical orders of the estimated two-photon absorption (2PA) coefficients and the intensity-dependent refractive index (n_2) were ~10^{-6} cm W^{-1} and ~10^{-7} cm^2 W^{-1}, respectively.

Received 11th December 2025
Accepted 10th February 2026

DOI: 10.1039/d5ra09607c

rsc.li/rsc-advances

Introduction

Nonlinear optical (NLO) materials are crucial for the development of next-generation photonic devices, including optical switches, limiters, modulators, and ultrafast lasers. Titanium dioxide (TiO_2), a wide-bandgap semiconductor (3.0–3.2 eV), is recognized for its chemical stability, high refractive index, and strong photocatalytic activity. However, pristine TiO_2 nanoparticles (NPs) exhibit relatively weak intrinsic third-order NLO responses, which limit their direct application in nonlinear photonic technologies. To overcome this limitation and enhance and tune the NLO properties of TiO_2 nanomaterials, researchers have extensively explored metal doping as an effective strategy. To improve the optical nonlinearity of TiO_2, it is doped with several metals, such as Bi, Au, Mn, Ag, and Pt, which shift its absorption to the visible spectral range. In particular, upon doping, the energy bandgap of TiO_2 nanomaterials is reduced to the visible range, which enhances the photocatalytic activity of TiO_2. The factors affecting the photocatalytic activity of metal-doped TiO_2 include the nature of the dopant, amount of the dopant used, preparation technique, and annealing and reductive treatments that are employed.[1–5] Doping TiO_2 NPs with transition or noble metals, such as Ag, Au, Cu, Fe, Ni, and Co, introduces localized electronic states within the bandgap, facilitating multiphoton absorption, charge transfer processes, and the enhancement of NLO susceptibilities. Metal dopants can induce localized surface plasmon resonance (LSPR) effects, especially in noble metals, such as Ag and Au, which strongly enhance the local electromagnetic field around NPs. This enhancement leads to a significant increase in the third-order nonlinear susceptibility ($\chi^{(3)}$), resulting in stronger nonlinear absorption (*e.g.*, reverse saturable absorption, RSA) and nonlinear refraction (*e.g.*, self-focusing or self-defocusing). Moreover, the incorporation of metal dopants alters the TiO_2 crystal lattice, introduces defect

[a]*Department of Physics, GSS, GITAM Deemed to be University, Visakhapatnam 530045, Andhra Pradesh, India. E-mail: gpodagat@gitam.edu; satgurusai.gk@gmail.com*

[b]*Department of Chemistry, GSS, GITAM Deemed to be University, Visakhapatnam 530045, Andhra Pradesh, India*

[c]*Medi-Valley, Andhra Pradesh Medtech Zone (AMTZ), Visakhapatnam, Andhra Pradesh, India*

[d]*School of Physics and DRDO Industry Academia – Centre of Excellence (formerly ACRHEM), University of Hyderabad, Hyderabad 500046, Telangana, India*

states, and modifies the polarizability of the material. These changes play a critical role in determining the nature and magnitude of nonlinear effects under high-intensity femtosecond (fs) or picosecond (ps) laser excitation. For example, Ag-doped TiO_2 NPs have demonstrated superior RSA behavior and enhanced nonlinear refractive indices, which are desirable for optical limiting applications. Similarly, iron (Fe)- and cobalt (Co)-doped TiO_2 systems exhibit strong third-order nonlinearity, attributed to the charge transfer between metal ions and the TiO_2 host, improved carrier lifetimes and trap-assisted nonlinear processes. Bi-doped TiO_2 NPs[6–14] modify the electronic band structure, carrier lifetimes, and light absorption, which enhance the photocatalytic activity.

Similarly, these systems exhibit good nonlinear properties due to the modified light absorption, carrier lifetimes, and band structures as both photocatalytic activity and nonlinear optical properties are influenced by the same mechanisms.[6–14] Moreover, co-doping Bi with other dopants has been demonstrated to enhance the photocatalytic activity for the efficient degradation of several pollutants, resulting from various metal symbiotic relationships.[15] In this study, bimetallic doping with Mn and Bi was performed to assess changes in the third-order NLO behavior. It is reported that metal ions, such as Mn, Co, and Ni, promote the grain growth and anatase-to-rutile phase transition of TiO_2.[16] It was evident from the reports that the concentration of the dopant has a significant influence on the activity of photocatalysts relevant to Mn-doped TiO_2.[17] The lifetimes of excited charge carriers are extended at low Mn doping concentrations (3 mol%), resulting in higher photocatalytic activity. On the other hand, as the Mn doping concentration exceeds a certain threshold, crystal defects form, leading to charge-carrier recombination, thereby decreasing the photocatalytic activity.[17] The Mn-doped TiO_2 NPs have been proven to be a promising photocatalyst that works with visible light to detoxify water from organic contaminants.[17] Numerous studies have also been conducted on Bi-doped TiO_2 and its effects on various aspects of TiO_2 NPs.[18,19]

In the present study, the NLO properties of TiO_2 NPs were investigated using ~150 fs laser pulses at an input wavelength of ~800 nm, with the Mn concentration held constant and Bi doping concentrations varied at 2.5%, 5%, and 10%. The NLO behavior of metal-doped TiO_2 NPs was investigated using the single-beam Z-scan technique, which provided detailed insights into both the sign and magnitude of nonlinear absorption and nonlinear refraction. With growing interest in integrated and ultrafast optical systems, metal-doped TiO_2 NPs are emerging as highly tunable and efficient platforms for NLO applications due to their ease of synthesis, environmental stability, and strong light–matter interactions. The co-doping of Mn and Bi into TiO_2 significantly modified the NLO properties by enhancing local-field effects and polarizability. On the other hand, Bi–Mn co-doping reduced charge-carrier recombination by improving charge-separation efficiency. In particular, Mn doping created deep trap states within the bandgap of TiO_2, which served as the centres for nonlinear optical transitions. When Bi was co-doped with Mn, shallow acceptor levels were generated, and these levels induced the hybridization of the 6s state of Bi and 2p state of oxygen (O), leading to light absorption and stronger nonlinear processes.

Experimental analysis

Synthesis of Bi–Mn co-doped TiO_2 NPs

In the present study, Bi and Mn were co-doped to TiO_2 at a constant Mn concentration and a varied Bi proportions 2.5%, 5%, and 10% using deposition and precipitation method. In step 1, accurately weighed quantities of bismuth nitrate pentahydrate [$Bi(NO_3)_3 \cdot 5H_2O$] and manganese nitrate tetrahydrate [$Mn(NO_3)_2 \cdot 4H_2O$] were dissolved in deionized water. The mixed solution was stirred continuously at room temperature until both salts were fully dissolved, yielding a clear, homogeneous dopant solution. In step 2, in a separate vessel, the titanium precursor, titanium isopropoxide (TTIP), was added to a suitable volume of ethanol under magnetic stirring. Mixing was carried out thoroughly for 15–20 minutes to ensure a uniform precursor solution. Under vigorous stirring, the Bi–Mn aqueous solution was slowly added dropwise to the titanium precursor mixture. This gradual addition facilitates even distribution of the dopants and prevents local precipitation, thereby promoting uniform incorporation into the titanium matrix. Once the dopant and precursor solutions are fully combined, the pH of the mixture is adjusted by adding sodium hydroxide (NaOH) dropwise as the third step. The addition was continued until the pH reached approximately 9–10. The increase in pH triggers the hydrolysis of titanium species, leading to the formation of a white to pale brown precipitate that indicates the co-precipitation of doped TiO_2 NPs. Stirring of the suspension was continued for an additional 4 hours at slightly elevated temperatures, ranging from 40 °C to 60 °C, to promote particle formation and growth. The resulting precipitate was kept undisturbed for 12 to 24 hours. This aging period promotes complete crystallization and enhances the structural stability of the nanoparticles. After aging, the precipitate was separated by centrifugation. The solid was rinsed thoroughly with deionized water, followed by ethanol to remove any remaining impurities, unreacted ions, or nitrates. The washed material was transferred to a drying oven and dried at 100 °C for approximately 12 hours to remove residual moisture. Finally, the dried powder was calcinated in a muffle furnace at a temperature of 400 °C for 3 hours in air to obtain the anatase phase TiO_2 NPs in which Bi and Mn are doped.

Bi–Mn co-doped TiO_2 NPs are diffused in pure ethanol, and their corresponding NLO properties were investigated by employing the single beam Z-scan experimental technique. The three different concentrations (2.5%, 5%, and 10%) of Bi–Mn co-doped TiO_2 NPs, on being submerged in the solvent (pure ethanol), produced a colloidal solution for the respective samples. The colloidal solutions at three different concentrations were ultrasonicated for 20 minutes to ensure their monodispersity. We used an air-tight container to preserve the colloidal solution and protect it from unwanted contamination and decomposition. UV-visible absorption spectroscopy was performed for the three co-doped Bi–Mn-TiO_2 NPs at different concentrations to observe the surface plasmon resonance. Field-emission scanning electron microscopy (FESEM) and high-resolution transmission electron microscopy (HRTEM)

were carried out to validate the uniform, distributive pattern (monodispersed) of TiO_2 NPs in ethanol. The lattice constant was determined from the assembled, patterned atomic lattice observed with a high-resolution transmission electron microscope (HRTEM). The average grain sizes of the co-doped Bi–Mn TiO_2 colloids were determined from FESEM images.

Single-beam Z-scan method

In the present work, co-doped Bi–Mn-TiO_2 NPs in three different proportions (2.5%, 5%, and 10%) were prepared using the wet-chemical technique, and their powders were dispersed in ethanol to prepare a uniformly distributed monodispersed colloidal solution. The open aperture (OA) and closed aperture (CA) traces of the readily produced Bi–Mn co-doped TiO_2 colloids in all three proportions were recorded using ultrashort laser pulses with a pulse duration of ~150 fs (~800 nm central wavelength, repetition rate of 76 MHz). The behavior of the three dopant concentrations was recorded using the Z-scan technique. The experimental CA Z-scan traces help us calculate the magnitude and signature of the intensity-dependent refractive index (n_2), whereas the OA Z-scan traces demonstrate the nonlinear absorption (NLA) of the samples. Z-scan experiments were performed with the laser beam diameter adjusted to ~4 mm, and the beam was focused with a plano-convex lens ($f = 100$ mm). The approximately projected beam waist ($\sim 2\omega_0$) at the focal location of the plano-convex lens was 50 μm. The peak intensity obtained at the focus was typically 600 MW cm^{-2}. A cuvette supported by a sample holder is utilized to contain the Bi–Mn co-doped TiO_2 colloids. A cuvette with a path length of ~1 mm containing colloidal dispersions was placed in the path of the laser beam on a translational stage. The sample was scanned by translating it along the Z-scan stage from $-10Z_0$ to $+10Z_0$, over the focal plane of the lens, where Z_0 is the Rayleigh range. The converged incident laser beam enters the Bi–Mn co-doped TiO_2 colloids in the cuvette in the sample holder. The transmitted laser beam through the sample was recorded with a photodiode. The motorized stage and the photodiode were interfaced to a computer *via* the LabVIEW software.

Results and discussion

UV-visible absorption spectroscopy

A spectrographic investigation of 2.5%, 5%, and 10% Bi–Mn co-doped TiO_2 is conducted and recorded at normal room temperature. Fig. 1(a) shows a red shift in the absorption peak of Bi–Mn co-doped TiO_2 NPs in ethanol. At 213 nm, absorption peaks were observed for all three different proportions of Bi–Mn-TiO_2. The energy of the three doped samples can be evaluated by the following equation:

$$E_g = 1240/\lambda_g, \quad (1)$$

where E_g depicts the energy bandgap, and λ_g is the absorption margin of the photocatalyst.[20] TiO_2 comprises the semiconductor NP properties, and as a consequence, it does not portray any signature of SPR. Fig. 1(b), (c), and (d) depict the Tauc plots for 2.5%, 5%, and 10% Bi–Mn co-doped TiO_2, respectively, acquired from the characterization of ultraviolet-visible spectroscopy. The Tauc method is a popular technique used to calculate the bandgap energy of semiconductor materials, as well as indicating whether the bandgap is direct or indirect.[21] The bandgap type can be identified from a Tauc plot by comparing the plots for different values of n ($n = 1/2$ and $n = 2$) and observing the plot that yields a clearer linear region and sharper bandgap transition.[21] In the Tauc plot, the quantity energy (eV) along the X-axis is plotted against $(\alpha h\nu)^{1/2}$ along the Y-axis. The curve obtained is intersected by a tangent that extends and meets a point on the X-axis (where $Y = 0$), which yields the resulting bandgap of the desired material. Pure TiO_2 NPs have a bandgap lying in the range of (3–3.2 eV)[22] whose equivalent wavelength lies in the UV spectral region.

Here in the present study, Tauc plots of all three samples, the plot of $(\alpha h\nu)^{1/2}$ *versus* energy, yield a linear region near the onset of absorption, indicating that all three different concentrations of Bi–Mn co-doped TiO_2 possess an indirect bandgap. Fig. 1(a) shows an absorption peak at ~213 nm, which is not the signature of Bi–Mn co-doped TiO_2 NPs, and in the determination of the optical bandgap, one cannot consider the signature of the solvent. The indirect bandgaps were estimated as ~3 eV for 2.5% Bi–Mn-TiO_2, ~2.7 eV for 5% Bi–Mn-TiO_2, and ~2.5 eV for 10% Bi–Mn-TiO_2. Increasing the doping concentrations of Bi and Mn results in a gradual decrease in the bandgap, thereby facilitating effective interactions of the photocatalysts with visible light. Doping of Bi reduces the bandgap and advances the establishment of further energy levels higher than the valence band of TiO_2.[23]

X-ray diffraction data

The diffractograms obtained for the 2.5%, 5%, and 10% Bi–Mn-TiO_2 are shown in Fig. 2(a), and the standard XRD spectrum of pure TiO_2 NPs in ethanol is shown in Fig. 2(b). The XRD spectrum indicates the presence of the anatase phase of TiO_2, as per JCPDS no. 00-021-1272. There may always be a small fraction of the utile phase, but we did not conduct any studies to filter out the residual rutile phase. This demonstrates that dopants Bi and Mn are successfully incorporated into the TiO_2 lattice. The traditional peaks of the phase anatase are consistently observed at positions of 2θ = 25.25°, 37.36°, 30.36°, 47.88°, 54.73°, 62.71°, and 75.30°. The Miller indices of the peaks, along with their associated 2θ values, are (101), (004), (012), (200), (211), (204), and (215), respectively. The anatase phase of TiO_2 has a broader bandgap compared with the rutile phase, and the anatase phase also exhibits a direct bandgap, which is another reason why TiO_2 is an effective photocatalyst and in optoelectronics.[24] Similarly, the peak near 27.4° corresponding to (110) may indicate the presence of the rutile phase of TiO_2 NPs. On the other hand, the small humps in the range 34°–35° indicate the presence of Bi and Mn in their oxide phases.

The average grain/crystallize size is estimated for the three different concentrations of Bi–Mn co-doped TiO_2 on the basis of XRD data through the Debye–Scherrer formula, as stated in eqn (2):

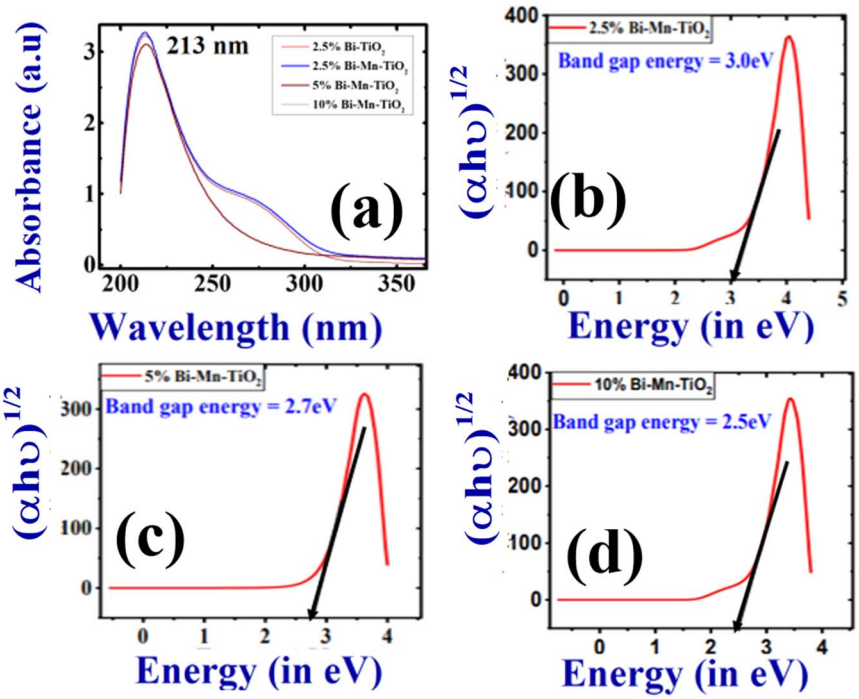

Fig. 1 (a) Ultraviolet-visible absorption spectra for 2.5%, 5%, and 10% Bi–Mn co-doped TiO_2 NPs dissolved in ethanol. (b–d) Tauc plots for 2.5%, 5%, and 10% Bi–Mn co-doped TiO_2 NPs.

$$D = K\lambda/\beta \cos\theta \quad (2)$$

The crystallite sizes obtained were ~6.62 nm, ~7.38 nm, and ~7.62 nm (shown in Table 1) for 2.5% doped Bi–Mn-TiO_2, 5% doped Bi–Mn-TiO_2, and 10% Bi–Mn-TiO_2, respectively.

Field emission electron microscopy (FESEM) characterization

The as-prepared Bi–Mn-TiO_2 NPs in three different doping proportions were morphologically investigated using the FESEM technique to gain a better understanding of the particle size and surface characteristics. The surface morphological features observed for all three different concentrations indicated spherical structures of Bi and Mn. Implantation of Bi and Mn into the TiO_2 lattice matrix did not have any significant impact on the crystal arrangement of TiO_2, as analyzed from XRD studies; however, particle binding was observed, could be due to the small size (nanometer scale) of the material,[25] as seen from Fig. 3(a), (e), and (i). We also performed energy-dispersive X-ray (EDX) to confirm the presence of Bi and Mn in the prepared material. The EDAX spectrum accurately identifies the energy signals of Bi and Mn, as well as those of Ti and O_2. This confirms that Bi and Mn were effectively confined within the TiO_2 photocatalyst.[21] Fig. 3(b), (c), (f), (g), (j), and (k) illustrate the FESEM images and their corresponding EDAX spectra of 2.5%, 5%, and 10% Bi–Mn co-doped TiO_2 NPs, respectively. The insets of Fig. 3(c), (g), and (k) demonstrate the weight percentages of 2.5%, 5%, and 10% Bi–Mn co-doped TiO_2 NPs, respectively. To construct the particle size histogram, FESEM images shown in Fig. 1 of the SI were utilized.

Fig. 3(d), (h), and (l) illustrate the effective grain sizes of 2.5% Bi–Mn co-doped TiO_2, 5% Bi–Mn co-doped TiO_2, and 10% Bi–Mn co-doped TiO_2, respectively. By employing the freely

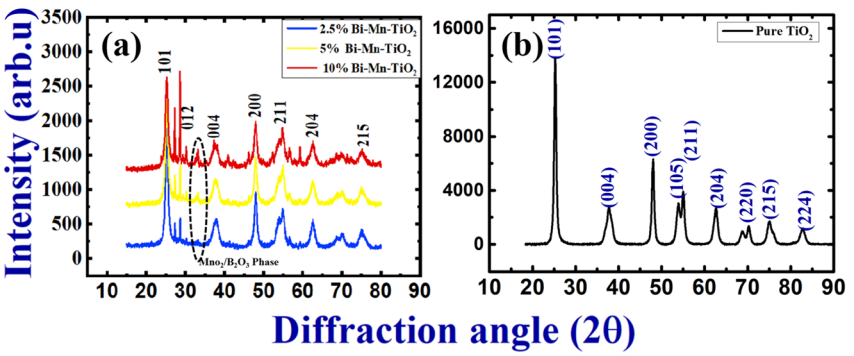

Fig. 2 (a) XRD spectra of 2.5% Bi–Mn-TiO_2 NPs, 5% Bi–Mn-TiO_2 NPs, and 10% Bi–Mn-TiO_2 NPs and their respective Miller indices. (b) Standard XRD spectrum of TiO_2.[30]

Table 1 Calculated average crystallite size and strain of 2.5%, 5%, and 10% Bi–Mn-TiO_2 NPs

Bi proportion	Peak position (2θ)	FWHM	Crystallite size (D) (nm)	D average (nm)	Strain
2.5% BMT	25.26	1.02	7.94	6.62	0.02
	37.76	1.53	5.50		0.02
	47.96	1.07	8.13		0.01
	54.51	2.01	4.44		0.01
	62.56	1.30	7.14		0.01
	75.20	1.53	6.57		0.01
5% BMT	25.25	1.03	7.94	7.38	0.02
	37.75	1.50	5.60		0.02
	47.95	1.06	8.17		0.01
	54.54	1.98	4.50		0.02
	62.55	1.31	7.10		0.01
	75.17	1.44	6.98		0.01
10% BMT	25.23	1.06	7.70	7.62	0.02
	27.20	0.73	11.14		0.01
	28.60	0.82	10.01		0.01
	32.96	0.83	9.97		0.01
	37.60	1.49	5.62		0.02
	40.88	0.67	12.67		0.01
	47.92	1.11	7.86		0.01
	54.52	2.25	3.97		0.02
	61.64	2.35	0.23		0.3
	62.51	1.32	7.03		0.01

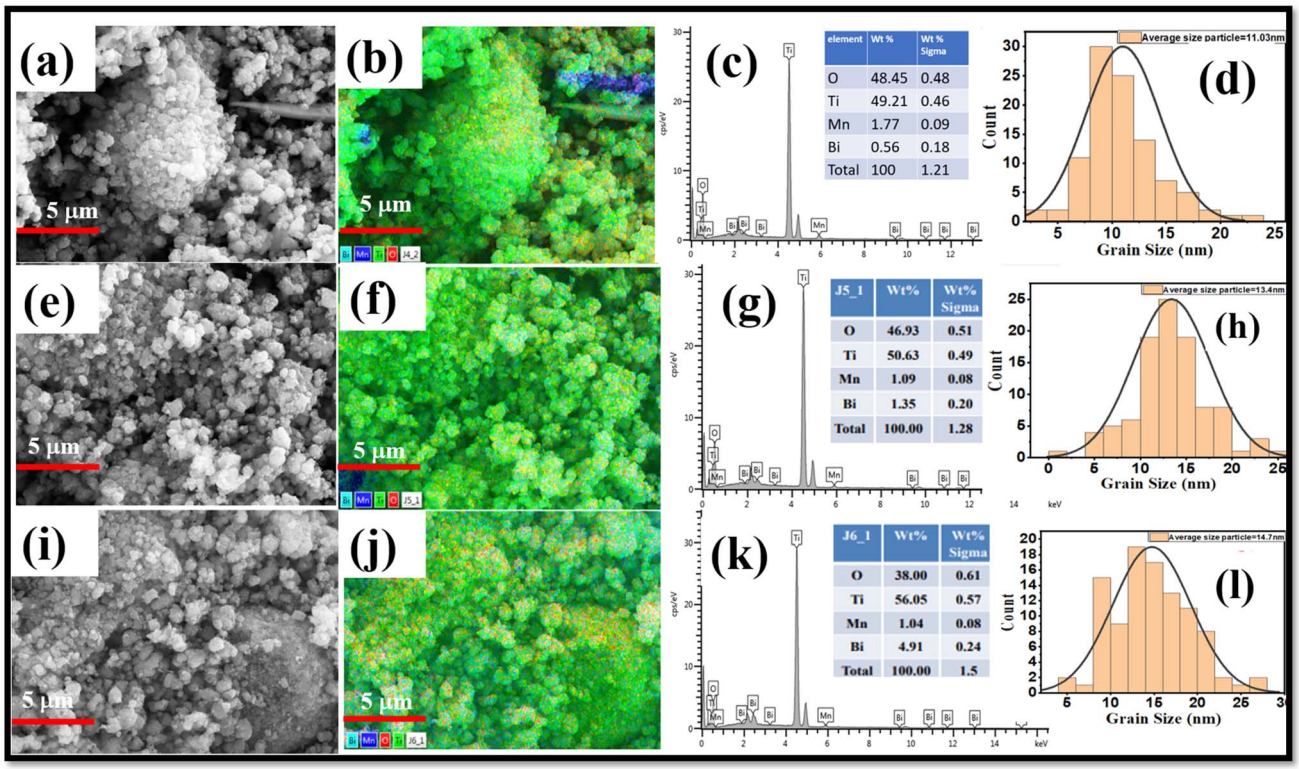

Fig. 3 (a) FESEM images of 2.5% Bi–Mn co-doped TiO_2 NPs. (b and c) EDAX images of 2.5% Bi–Mn co-doped TiO_2 NPs. Inset shows the wt% of Bi, Mn, Ti, and oxygen. (d) Histogram constructed from FESEM, predicting the average crystallite size to be ~11 nm. (e) FESEM images of 5% Bi–Mn co-doped TiO_2 NPs. (f and g) EDAX images of 5% Bi–Mn co-doped TiO_2 NPs. Inset shows the wt% of Bi, Mn, Ti, and O. (h) Histogram constructed from FESEM, predicting the average crystallite size to be ~13.5 nm. (i) FESEM images for 10% Bi–Mn co-doped TiO_2 NPs. (j and k) EDAX images of 10% Bi–Mn co-doped TiO_2 NPs. Inset shows the wt% of Bi, Mn, Ti, and O. (l) Histogram constructed from FESEM, indicating the average crystallite size to be ~14.7 nm.

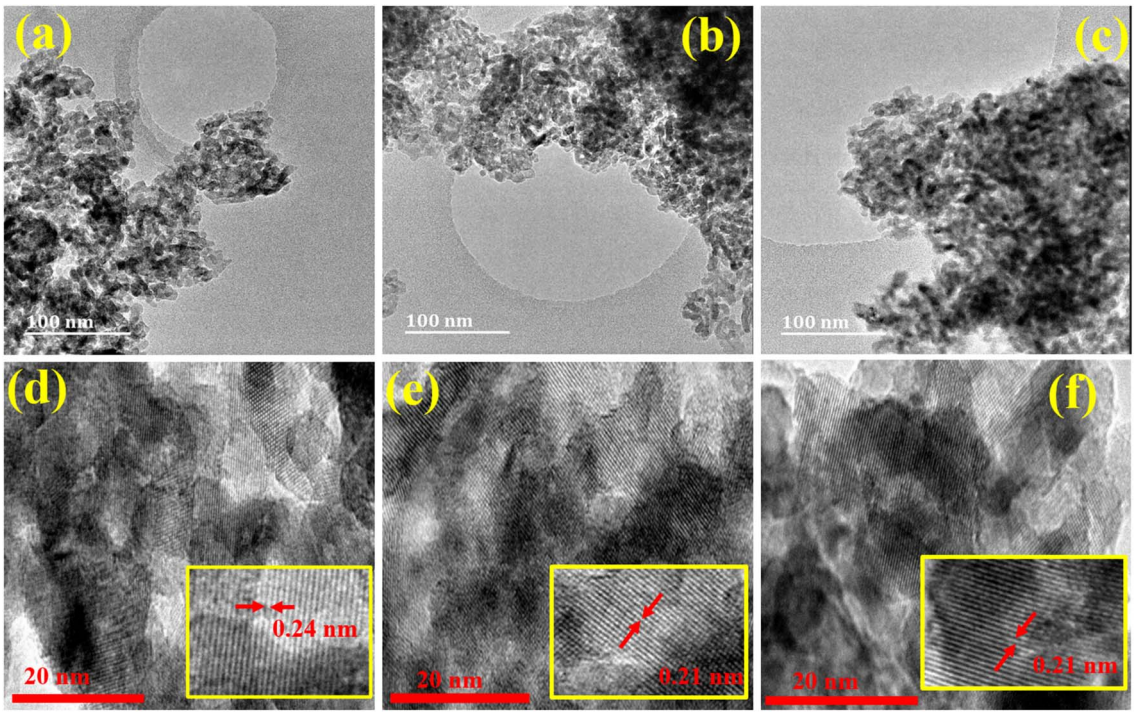

Fig. 4 (a) TEM image of 2.5% Bi–Mn co-doped TiO_2 NPs. (d) HRTEM image; inset showing a lattice spacing of 0.24 nm. (b) TEM image of 5% Bi–Mn co-doped TiO_2 NPs. (e) HRTEM image; inset showing a lattice spacing of 0.21 nm. (c) TEM image of 10% Bi–Mn co-doped TiO_2 NPs. (f) HRTEM image; insets of (d–f) showing a lattice spacing of 0.21 nm.

available online software 'ImageJ', we could estimate the average crystallite sizes by constructing a histogram. In the next step, a histogram for grain distribution size was created using the Origin software. Subsequently, the histograms attained were appropriately fitted with the bell-shaped Gaussian profile function using the Origin software. After a few iterations, the fitted peak showed an acceptable R^2 (0.99). The evaluated average grain/particle sizes of the 2.5% Bi–Mn-TiO_2, the 5% Bi–Mn-TiO_2, and the 10% Bi–Mn-TiO_2 are ~11.03 nm, ~13.4 nm, and ~14.7 nm, respectively.

Transmission electron microscopy (TEM) characterization

Fig. 4(a), (d), (b), (e), (c), and (f) present the TEM characterization of 2.5% Bi–Mn co-doped TiO_2 NPs, 5% Bi–Mn co-doped TiO_2 NPs, and 10% Bi–Mn co-doped TiO_2 NPs, respectively. The TEM analysis provides a clearer, deeper understanding of the crystal structure's morphology. The TEM images presented clearly and accurately depict the impregnated Bi and Mn nanoparticles within the TiO_2 lattice. The measured lattice spacing *via* HRTEM imaging demonstrates that the 0.24 nm/0.21 nm spacing [shown as insets in Fig. 4(d)–(f)] is specific to the anatase phase of TiO_2 NPs, and that the dopants are precisely doped into the intended sites.

Ultrafast Z-scan studies of Bi–Mn co-doped TiO_2 NPs in ethanol

The ultrafast Z-scan approach is well-suited for examining the NLO properties of the material. Z-scan analysis provides data on the Kerr (nonlinearity) strength. Additionally, the Kerr (nonlinearity) effect is defined as the measure of the refractive index (nonlinear) (n_2) of a given optical material. One can easily obtain the magnitude of the third-order positive nonlinear susceptibility ($\chi^{(3)}_{\text{effective}}$) or negative nonlinear susceptibility of the desired material by employing the single beam-Z-scan technique. Using a femtosecond (fs) laser, non-linear optical analysis is carried out on Bi–Mn co-doped TiO_2 colloids submerged in ethanol. The parameters of the ultrashort pulses produced by an fs laser (Chameleon, M/s Coherent, USA) include a central wavelength of ~800 nm, repetition rate of ~76 MHz, and a pulse duration of ~150 fs. These ultrashort pulses (after focusing) were allowed to pass through the ultrasonicated the Bi–Mn-TiO_2 colloids in ethanol, which were kept in a quartz cuvette with a pathlength of ~1 mm.

The Z-scan technique involves scanning three different colloidal samples prepared on the Z-scan platform (or motorized stage) using a focused Gaussian beam. A focused Gaussian beam is converged with the help of a convex lens. Throughout the scanning process, the evolution of the Gaussian beam's electric field was accounted for. The electric field of the laser pulses produced is analogous to the functional reliability in terms of position and radial stretch from the core region of the Gaussian beam, which can be evaluated using the equation below:

$$I(Z,r) = \frac{1}{1+\left(\frac{Z^2}{Z_R{}^2}\right)} e^{\left[\left(\frac{-2r^2}{\omega^2(Z)}\right)+\left(-\frac{t^2}{\tau_p{}^2}\right)\right]} I_O, \quad (3)$$

where I_0 denotes the irradiance at the focus ($Z = 0$), $Z_R = \frac{\pi\omega_0{}^2}{\lambda}$ is defined as the Rayleigh range, τ_p can be explained as the duration of the laser pulses. $\omega(Z)$ denotes the beam waist of the incoming laser beam at any point of Z, and the modification in the waist of the beam in a way that follows the place of Z is represented by:

$$\omega^2(Z) = \omega_0{}^2\left(1 + \frac{Z^2}{Z_R{}^2}\right), \quad (4)$$

where ω_0 is defined as the beam radius at the focal point ($Z = 0$) of a convex lens.

Z-scan (OA) open aperture studies

The incoming laser beam is focused and allowed to pass through Bi–Mn co-doped TiO_2 NP samples in ethanol, held in a quartz cuvette (~1 mm path length). The three co-doped samples are scanned along the Z-scan platform, which is managed using the LabVIEW software. The modifications in the laser intensity directly correlate with the earlier and later positions of the three co-doped samples relative to the focal point of the converging lens. The interaction (whether transmission or absorption) of the three samples and the laser beam changes based on the Z-position, as represented in eqn (5).[26] The evaluation and insight into the non-linear absorption (NLA) action depend upon the solution of the following equation:

$$\frac{dI}{dZ} = -\alpha(I)I(z), \quad (5)$$

Such that

$$\alpha(I) = \alpha_0 + \beta I + \gamma I^2\ldots, \quad (6)$$

where two-photon absorption (2PA) coefficients are denoted by 'β', and three-photon absorption (3PA) coefficients are denoted by 'γ' accordingly. Moreover, $\alpha(I)$ defines the intensity of the reliable optical total absorption coefficient (NLA).

The OA transmittance (normalized) of the Z-scan technique is represented by eqn (7)[26] as follows:

$$(Z) = \sum_{m=0}^{\infty} \frac{[(-q_0(Z,0))]^m}{(m+1)^{\frac{3}{2}}}, \quad (7)$$

Such that

$$q_0(Z,0) = \frac{\beta I_0 L_{eff}}{\left(1 + \frac{Z^2}{Z_0{}^2}\right)}, \quad (8)$$

where I_0 is defined as the intensity of the laser peak at the focus of the beam.

$$L_{eff} = \frac{(1 - e^{\alpha_0 L})}{\alpha_0}, \quad (9)$$

where L is denoted by the length of the sample, and Z is defined as the location of the sample with reference to the focal point. α_0 is denoted as the sample's linear absorption coefficient, and Z_0 is defined as the Rayleigh's length of the focused laser beam.

We can retrieve the NLA coefficients by fitting the OA data according to eqn (3) and (4). Normally, the NLA activity includes saturable absorption (SA) and reverse saturable absorption (RSA), which has been examined elsewhere.[26] Over time, situations may arise due to increased peak intensity, particularly in areas with pure SA or RSA curves, leading to a shifting behavioral pattern from SA to RSA or RSA to SA. Earlier, in the OA Z-scan, when a shifting behavioral pattern from SA to RSA is observed, it is assumed to be the collaborative behavior of two-photon absorption (2PA), along with SA. Henceforth, mathematically, the total (NLA) is fitted according to the proposed model by Ganeev *et al.* as stated in eqn (10):[27]

$$\alpha(I) = \frac{\alpha_0}{(1 + I/I_S)} + \beta I, \quad (10)$$

where 'I_S' denotes the saturation intensity (GW cm^{-2}), and β is designated as the 2PA coefficient (cm GW^{-1}). The first term in eqn (10) suggests the saturable intensity, and the second term implicates the 2PA coefficients.[28]

Fig. 5 depicts the OA traces of Bi–Mn co-doped TiO_2 NPs in ethanol recorded with 800 nm pulses, with (a) showing the data for 2.5% BMT, (b) showing the data for 5% BMT, and (c) showing the data for 10% BMT. All three studies were conducted at the same input power (*i.e.*, ~3 mW) and under the same experimental conditions. The recorded data and the theoretical fits for 2.5% Bi–Mn-TiO_2 NPs in ethanol show that Fig. 5(a) demonstrates a switching behaviour from saturable absorption (SA) to reverse saturable absorption (RSA) [RSA in SA] with an estimated two-photon absorption (2PA) coefficient of 1.05×10^{-6} cm W^{-1} and an intensity of saturation (I_S) of 5×10^5 W cm^{-2}. Similarly, the recorded data and it's theoretical fits for 5% Bi$MTiO_2$ NPs in ethanol shows as in Fig. 5(b), demonstrating a complex behavior, SA in RSA in SA with a two-photon absorption (2PA) coefficient ~1.05×10^{-6} cm W^{-1}, and a saturation intensity (I_S) of ~5×10^5 W cm^{-2}. Fig. 5(c) again depicts the OA data recorded at 800 nm with ~3 mW input power, along with the theoretical fits for 10% Bi–Mn-TiO_2 NPs in ethanol. It exhibits RSA switching behavior in SA, with a two-photon absorption (2PA) coefficient of ~2.95×10^{-7} cm W^{-1} and an intensity of saturation (I_S) ~ 4×10^6 W cm^{-2}.

SA is observed at low input intensities due to ground-state bleaching. In this regime, photons are absorbed by the ground-state electrons of NPs, promoting electrons from the valence band to the conduction band. As the electronic population of ground-state becomes depleted (*i.e.*, bleached), the material's absorption decreases. Incorporating Bi and Mn dopants into TiO_2 NPs will likely introduce intermediate energy states, which can facilitate faster excitation and enhance ground-state bleaching even at relatively low intensities. At higher input intensities, reverse saturable absorption (RSA) becomes the dominant mechanism. This occurs primarily *via* excited-state absorption (ESA) or free-carrier absorption (FCA) mechanisms. Electrons excited to intermediate or conduction band states can further absorb photons, thereby increasing the overall absorption. Dopants such as Bi and Mn are known to introduce deep trap states or intermediate bands, thereby significantly enhancing these nonlinear processes. Unlike pure

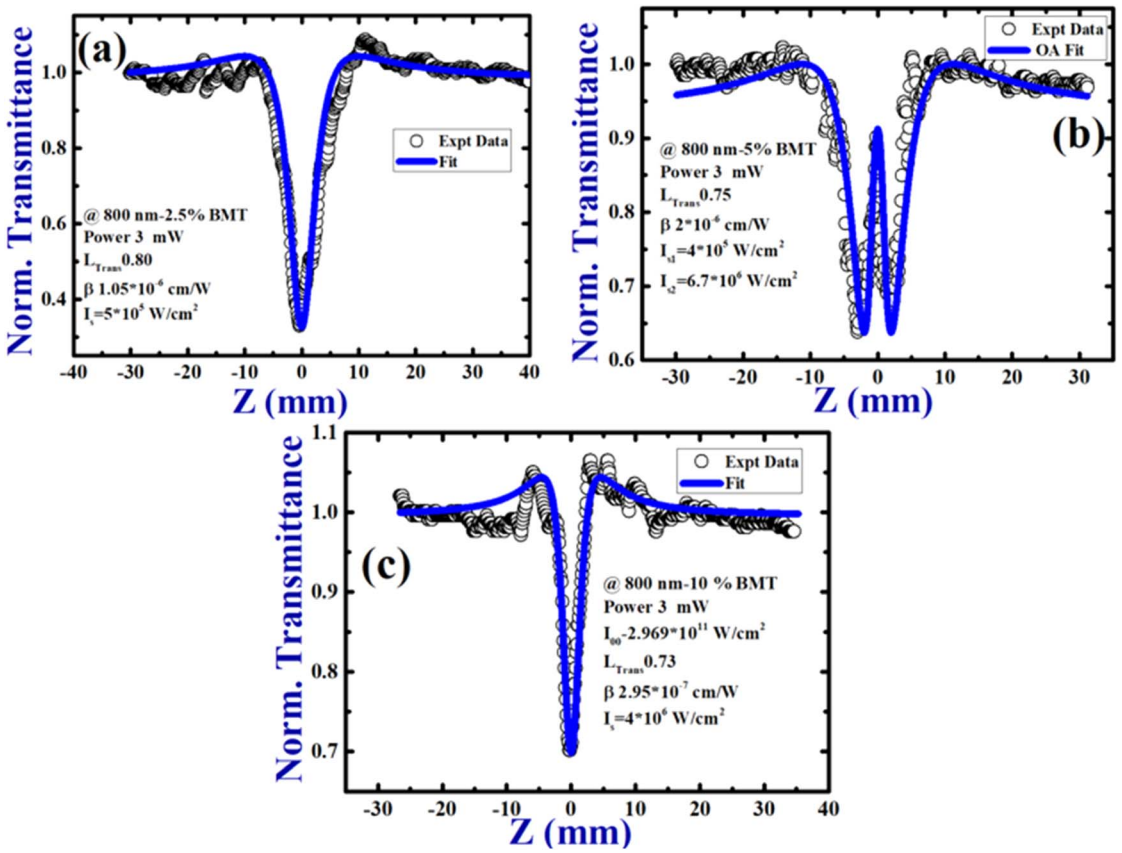

Fig. 5 OA traces of Bi–Mn co-doped TiO_2 NPs in ethanol recorded with 800 nm input wavelength, ~150 fs pulse duration, and a repetition rate of ~76 MHz: (a) 2.5% BMT, (b) 5% BMT, and (c) 10% BMT. Open circles denote the experimental data and blue solid lines represent the theoretical fits.

SA or RSA behavior, the switching characteristics observed, as depicted in Fig. 5(a)–(c), suggest the presence of multiple competing nonlinear mechanisms. For instance, in an SA → RSA transition, the ground state initially bleaches (SA), but as the excited states become populated, ESA dominates, leading to RSA. In a more complex RSA → SA → RSA sequence, the material may first show RSA or nearly linear behavior at very low intensities, then SA due to trap-state saturation and ground-state bleaching, and then revert to RSA at higher intensities as ESA becomes the prevailing process. Bi (Bi^{3+}) likely introduces localized states near the conduction band, which can support multi-photon or excited-state absorption pathways. Manganese (Mn^{2+}/Mn^{3+}), owing to its multiple valence states, may contribute to charge-transfer transitions and the formation of trap states, thereby enhancing both SA and RSA responses at varying excitation intensities. Overall, the observed OA Z-scan traces may be attributed to a combination of trap-state saturation, multiphoton absorption, and complex band-structure modifications induced by Bi–Mn co-doping, which together contribute to the rich and dynamic nonlinear optical behavior of the material.

Closed aperture (CA) Z-scan studies

We have performed a CA Z-scan of Bi–Mn co-doped TiO_2 NPs dispersed in ethanol to investigate the nonlinear refraction (NLR) behaviour. Theoretically, the CA Z-scan adjustment comprises a transmission curve[26] that is depicted in eqn (11):

$$T_{CA} = 1 \pm \frac{4\Delta\Phi\left(\frac{z}{z_0}\right)}{\left[\left(\frac{z}{z_0}\right)^2 + 9\right]\left[\left(\frac{z}{z_0}\right)^2 + 1\right]} \quad (11)$$

Moreover, in CA curves, the difference between the normalized peak and the normalized valley is

$$\Delta T_{p-v} = 0.406(1 - S)^{0.25}|\Delta\Phi_0|,$$

where S is designated as OA transmittance. The non-linear parameters, namely two photon absorption coefficient (2PA) depicted as β (cm GW^{-1}), three photon absorption coefficient (3PA) depicted as γ (cm^2 GW^{-3}), and refractive index non-linear in nature depicted by n_2 (cm^2 GW^{-1}). Furthermore, the non-linear absorption cross-section (σ), the real third-order value of susceptibility $\chi^{(3)}$, and the imaginary third-order value of $\chi^{(3)}$ of three given co-doped colloidal samples can also be evaluated.

The n_2 that is of order 2 can be evaluated through eqn (12):

$$n_2\ (cm^2\ W^{-1}) = \frac{\Delta\Phi}{I_0 \times L_{eff} \times k} = \frac{\Delta\Phi \times \lambda}{I_0 \times L_{eff} \times 2\pi} \quad (12)$$

To estimate the real and imaginary $\chi^{(3)}$, the expressions are explained as $\mathrm{Im}|\chi^{(3)}|\ (\mathrm{m^2\ V^{-2}}) = \frac{c\varepsilon_0\lambda {n_0}^2\alpha_2\ (\mathrm{m\ W^{-1}})}{2\pi}$ and $\mathrm{Re}|\chi^{(3)}|\ (\mathrm{m^2\ V^{-2}}) = 2c\varepsilon_0 {n_0}^2 n_2\ (\mathrm{m^2\ W^{-1}})$ respectively, and the third-order nonlinear susceptibility $\chi^{(3)}$ can be deduced for real values of $\chi^{(3)}$ as well as imaginary values of $\chi^{(3)}$. The modified association is given as $|\chi^{(3)}|\ (\mathrm{e.s.u.}) = \frac{(3\times10^4)^2|\chi^{(3)}|\ (\mathrm{m^2\ V^{-2}})}{4\pi}$, which helps in switching between varying units.

Fig. 6 shows the CA traces and the fitted data of Bi–Mn co-doped TiO_2 NPs in ethanol, recorded with 800 nm at an input power of 1.5 mW. Fig. 6(a) depicts the recorded experimental CA data of 2.5% Bi–Mn co-doped TiO_2 NPs in ethanol and its theoretical fitting, with an estimated intensity-dependent refractive index (n_2) of -5.74×10^{-8} $\mathrm{cm^2\ W^{-1}}$. Fig. 6(b) depicts the recorded experimental CA data of 5% Bi–Mn co-doped TiO_2 NPs in ethanol, and its theoretical fitting, with an estimated intensity-dependent refractive index (n_2) $\sim -1.857\times10^{-7}$ $\mathrm{cm^2\ W^{-1}}$. Fig. 6(c) depicts the recorded experimental CA data for 10% Bi–Mn co-doped TiO_2 NPs in ethanol and its theoretical fit, with an estimated intensity-dependent refractive index (n_2) $\sim -1.7\times10^{-7}$ $\mathrm{cm^2\ W^{-1}}$. Unlike OA traces, CA traces show fluctuations in the recorded data. Although the experiment was repeated, the recorded data is essentially the same. We could pick the best possible data, but we ended up with the data shown. The NLO characteristics of TiO_2 NPs were studied by the researchers, but they are individually doped with either Bi or Mn. The reported studies are also very limited on Bi–Mn co-doped TiO_2 NPs. In our group, we have been working on the NLO characterizations of TiO_2 NPs doped with different metals, such as Au[29] and Bi,[30] and have reported our findings. Particularly in the case of Bi, the OA studies performed at 800 nm demonstrated a very complex behavior.[30] In this study, along with the doping of Bi, Mn is also present, which modifies the electronic structure and the intermediate defect states. Consequently, a different NLO behaviour was evident in the present study. Bousiakou *et al.*[31] have reported on the variation of optical properties of anatase TiO_2 upon the doping of Mn. In their studies, they discussed modifying the energy levels of TiO_2 NPs; however, their focus was particularly on cosmetic applications. Caligulu *et al.*[32] have reported the surface morphology and optical properties of Ca and Mn-doped TiO_2 nanostructured thin films. In a previous work, we evaluated the thermal nonlinearity caused by Ag doping in TiO_2 NPs and reported using high-repetition-rate pulses.[33]

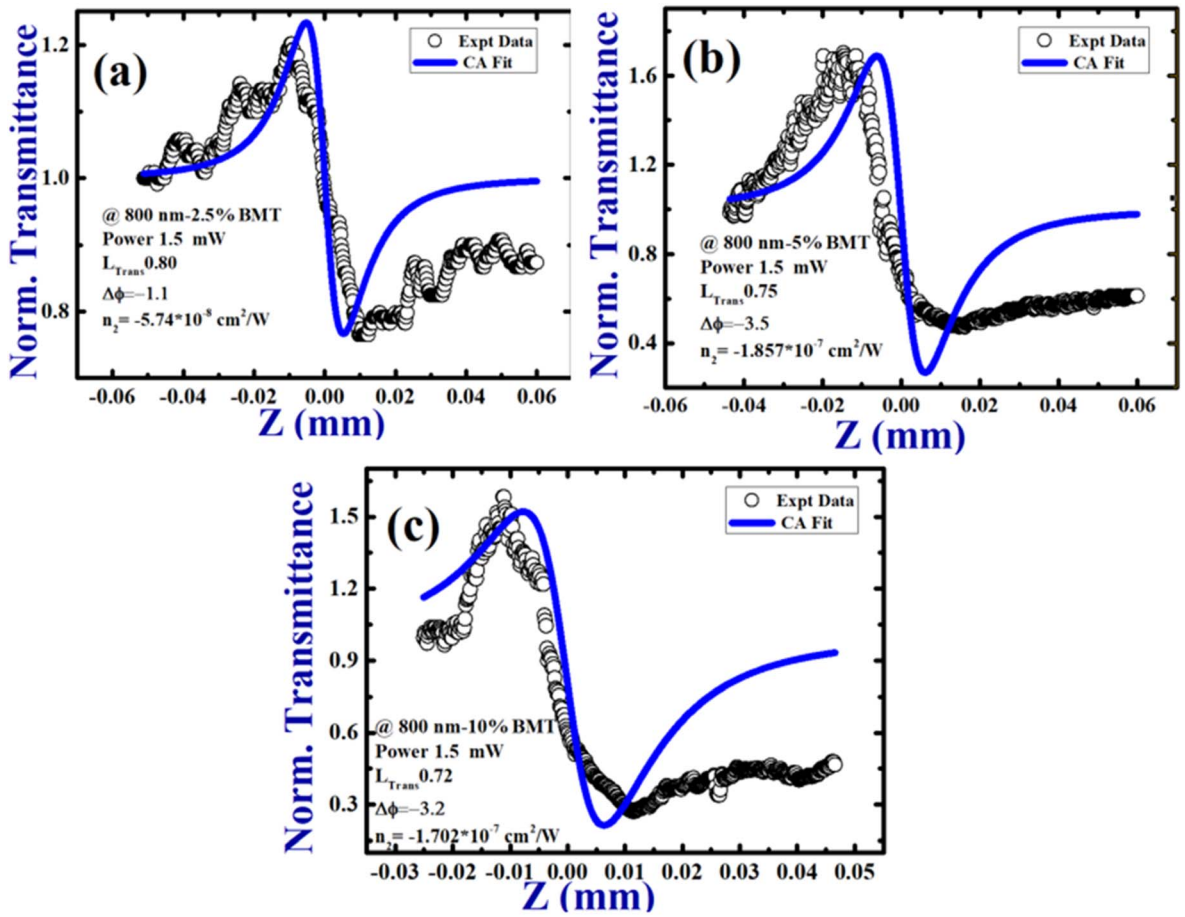

Fig. 6 CA curves of (a) 2.5%, (b) 5%, and (c) 10% Bi–Mn co-doped TiO_2 NPs in ethanol, carried out with 800 nm input wavelength at 300 MW $\mathrm{cm^{-2}}$. Open symbols represent the experimental data, while the solid lines represent the theoretical curve fits.

In this study, the nonlinearity caused by thermal effects might also be present, as we performed our experiment with pulses delivered by the oscillator at a repetition rate of ~76 MHz. However, there is no literature on Bi–Mn co-doped NPs for NLO applications. Depending upon the repetition rate of the delivered laser pulses employed in the Z-scan experiment, one can superficially figure out the origin of nonlinearity, whether it is of electronic or thermal contribution. The thermal contribution is due to the accumulated thermal load and thermal lensing caused by the continuous impact of laser pulses at a high repetition rate (76 MHz). Consequently, the thermal loading caused by laser pulses leads to a temperature-dependent refractive index, $\frac{dn}{dT}$ has a slow response. For laser pulses delivered at a low repetition rate (1 kHz), the sample medium under consideration is provided with a time of ~1 ms, which is sufficient to relax from thermal loading. Consequently, the pure electronic nonlinearity is evident in this case.

To quantify the thermal contribution to the nonlinearity, one has to employ optical choppers that vary/modulate the repetition frequency, which clearly distinguishes the fast electronic response at all optical chopper duty cycles; however, the slow thermal response disappears at high duty cycles. In addition to the laser pulse repetition frequency, the pulse duration is crucial for determining thermal lensing, and hence, the thermal contribution to the nonlinearity. In particular, pulses with nanosecond and typically sub-nanosecond (~1 ps) durations are so long that thermal loading prevails.

Thermo-optic model fitting of the CA curve

To examine the thermal contributions to nonlinear absorption and refraction, the experimentally obtained CA trace was analyzed by fitting it to a theoretical model that accounts for the thermally induced refractive index change (Δn) arising from two- or higher-order multiphoton absorption processes. Under steady-state conditions, the normalized transmittance can be expressed as ref. 34–36. The origin of nonlinear absorption, either thermally or electronically, is the comparison of thermo-optical fitting parameters β_{Th} (2PA), obtained from the fitting of CA experimental data with the following mathematical relations,

$$T_{CAth} = 1 + \frac{\theta(\eta)}{\eta} \frac{1}{\left(1 + \left(\frac{z}{z_0}\right)^2\right)^{\eta-1}} \tan^{-1}\left(\frac{2\eta\left(\frac{z}{z_0}\right)}{2\eta + 1 + \left(\frac{z}{z_0}\right)^2}\right), \quad (13)$$

where η is the order of the absorption process and θ is the parameter that combines the contributions of the multi-photon absorption cross-section, laser repetition rate, and thermo-optic coefficient.

$$\theta(\eta) = L_{eff} \frac{\eta h\nu (N\sigma_\eta) H(\eta) f}{\lambda K} \frac{dn}{dT} \left(\frac{2}{\pi\omega_0^2}\right)^{\eta-2} \quad (14)$$

with

$$H(\eta) = \int_0^\tau (P(t))^\eta dt,$$

where $P(t)$ is the instantaneous power of the laser, $h\nu$ is the photon energy, N is the electron density (cm^{-3}), and K is the coefficient of thermal conductivity.

The nonlinear refractive index (n_2) and thermo-optical coefficient values in the fs regime were evaluated by the following relations:[36]

$$n_2 = \frac{\Delta n}{I_{00}} \quad (15)$$

$$\frac{dn}{dT} = \Delta n \frac{4K}{I_{00}\alpha_0\omega_0^2} \quad (16)$$

In our previous studies,[37] NLO studies of Al-doped Pt NPs in isopropyl alcohol (IPA) were performed using ~150 fs laser pulses at a repetition rate of ~76 MHz.[4] It was observed that the retrieved β_{th} was far higher than the β values obtained from OA Z-scan ($S = 1$) data, with a ratio of $\beta_{th}/\beta = 223$ at 700 nm wavelength. The higher value of $\beta_{th}/\beta = 223$ is due to the decrease of the obtained β with the huge variation of β_{th}, which designates the minimal thermo-optical effect in the nonlinear absorption.[36] Therefore, we believe that the NLA is mostly due to intra-band transitions, excited-state absorption, and charge-transfer effects. In our earlier work, the NLO properties of Al-doped Pt NPs dispersed in isopropyl alcohol were investigated using ~150 fs laser pulses at a repetition rate of ~76 MHz.[37] The extracted thermal nonlinear absorption coefficient (β_{th}) was found to be significantly larger than the nonlinear absorption coefficient (β) obtained from open-aperture (OA) Z-scan measurements ($S = 1$). At a wavelength of 700 nm, the ratio β_{th}/β was as high as 223. This large β_{th}/β ratio arises from the substantial reduction in the measured β relative to the pronounced variation in β_{th}, indicating a minimal contribution of thermo-optical effects to the observed nonlinear absorption.[36] Consequently, the nonlinear absorption is predominantly governed by intraband transitions, excited-state absorption, and charge-transfer mechanisms. Based on our previous work with the same laser credentials, we conclude that the observed nonlinearity is mostly of electronic origin rather than thermo-optical effects.

To provide a quantitative assessment of the differences between the thermal and electronic origins of nonlinearity in Bi–Mn co-doped TiO_2 NPs in ethanol, one must perform single-beam Z-scan studies with fs pulses at a repetition rate of ~1 kHz at different wavelengths, in addition to the NLO studies with high repetetion rate pulses (76 MHz).

Advantages of Bi–Mn co-doping into TiO_2 NPs

The NLO response of TiO_2 NPs is strongly governed by dopant-induced alterations in electronic structure, defect density, and charge-transfer dynamics. In mono-doped systems such as Au- and Bi-doped TiO_2, enhancement of NLO properties arises from distinct yet intrinsically limited mechanisms. For Au-doped TiO_2, the enhancement in nonlinear absorption and

refraction is predominantly attributed to the localized surface plasmon resonance (LSPR) of Au NPs. The resulting local electromagnetic field amplification enhances two-photon absorption (2PA) and excited-state absorption (ESA), thereby improving optical limiting behavior. However, this plasmon-driven enhancement is highly wavelength-selective, sensitive to thermal effects, and critically dependent on Au particle size and spatial distribution. In addition, plasmon-induced heating introduces significant thermo-optical nonlinearities, which can mask the intrinsic electronic NLO response. In contrast, Bi-doped TiO_2 exhibits enhanced NLO behavior mainly due to bandgap narrowing, the formation of Bi-related impurity states, and increased defect-assisted electronic transitions. The presence of Bi^{3+} ions, characterized by lone-pair electrons, induces lattice distortion within the TiO_2 matrix and facilitates intraband transitions and charge-transfer processes. Although this results in improved nonlinear absorption relative to pristine TiO_2, the overall enhancement is constrained by limited modulation of carrier lifetimes and the absence of magnetic or spin-assisted interactions.

By comparison, Bi–Mn co-doped TiO_2 NPs demonstrate a pronounced synergistic enhancement of the NLO coefficients that exceeds those of mono-doped systems. Bi contributes to bandgap narrowing and defect-mediated transitions, while Mn, through its multiple accessible oxidation states (Mn^{2+}/Mn^{3+}/Mn^{4+}), introduces efficient carrier trapping and hopping pathways. This cooperative modulation substantially increases the density of intermediate energy levels within the bandgap, thereby strengthening nonlinear absorption. Furthermore, Mn-related d–d transitions in conjunction with Bi-induced impurity states prolong excited-state lifetimes, leading to enhanced ESA and reverse saturable absorption (RSA). This electronic-driven mechanism is significantly more effective and stable than the plasmon-assisted enhancement observed in Au-doped TiO_2. Importantly, Bi–Mn co-doping suppresses dominant thermal contributions and favors electronic nonlinearities, enabling more reliable extraction of intrinsic NLO parameters such as the nonlinear absorption coefficient (β) and nonlinear refractive index (n_2). The absence of LSPR-dependent effects renders the Bi–Mn co-doped system less wavelength-restrictive and thermally robust, making it well suited for broadband optical limiting and ultrafast photonic applications. Consequently, the concurrent enhancement in nonlinear absorption and controlled nonlinear refraction yields a superior NLO figure of merit, establishing Bi–Mn co-doped TiO_2 as a more promising candidate for practical NLO device applications than its mono-doped counterparts.

To quantify defect states and trap levels, one must perform exclusive DFT calculations, which yield the intermediate states and their energies. However, the theoretical concept of defect/trap states is drawn from the existing/recent literature. As our interest is in improving the magnitudes of the nonlinear coefficients, we focused less on the quantitative analysis of the aforementioned defect/trap states using DFT techniques. Moreover, the limited time frame of our studies did not support the simulations during this work. Apart from this, literature is not available on the NLO of Bi–Mn co-doped TiO_2 NPs, though some reports are available on the individual effect of metal doping to TiO_2 NPs. No quantitative analysis was reported elsewhere on the NLO of Bi–Mn co-doped TiO_2 NPs, except for some schematic explanations on the "defect states" or "trap states".

Conclusions

In conclusion, we explored the NLO properties of ethanol-dispersed titanium dioxide (TiO_2) colloidal nanoparticles (NPs) co-doped with Bi and Mn. The Bi–Mn co-doped TiO_2 NPs were prepared by a deposition and precipitation method. Metal doping, particularly with Bi and Mn, enhances the photo response of TiO_2, making it attractive for applications in solar cells, catalysis, and phototherapy. Co-doping reduced the anatase phase bandgap from 3.2 eV to 3.0, 2.7, and 2.5 eV at the doping levels of 2.5%, 5%, and 10% Bi–Mn, respectively. Z-scan experiments, including OA and CA modes at 800 nm, were conducted, and the nonlinear optical coefficients were estimated. The OA Z-scan data showed complex NLO behavior, *i.e.*, SA switching to RSA and *vice versa*. The estimated effective 2PA coefficients were of the order of 10^{-6} cm W^{-1}. The CA scan data revealed negative nonlinear refractive index values, indicating self-defocusing effects due to the intensity-dependent refractive index of the order of $\sim 10^{-7}$ cm^2 W^{-1}.

Author contributions

TJ: writing – original draft, methodology, formal analysis, and data curation. SM: writing – original draft, resources, and methodology. SH: formal analysis and writing – original draft. SKV: formal analysis. CSA: writing – original draft. VRS: formal analysis and writing – original draft. GKP: conceptualization, writing – review and editing, writing – original draft, formal analysis, data curation, validation, supervision, software, project administration, methodology, investigation, and funding acquisition.

Conflicts of interest

The authors declare no conflicts of interest with any member of any organization.

Data availability

Data will be made available upon request.

Supplementary information (SI): FESEM images. See DOI: https://doi.org/10.1039/d5ra09607c.

Acknowledgements

The authors acknowledge the support from the DIA-CoE LASER Labs [formerly the Advanced Centre for Research in High Energy Materials (ACRHEM)], University of Hyderabad, funded by the DRDO, India, for providing the LASER LAB slots.

References

1 D. P. Macwan, P. N. Dave and S. Chaturvedi, A review on nano-TiO_2 sol–gel type syntheses and its applications, *J. Mater. Sci.*, 2011, **46**, 3669–3686, DOI: 10.1007/s10853-011-5378-y.

2 T. Liu and H. Zhang, Enhanced active oxidative species generation over Fe-doped defective TiO_2 nanosheets for boosted photodegradation, *RSC Adv.*, 2013, **3**, 16255–16258, DOI: 10.1039/d0ra08116g.

3 T. Huang, S. Mao, J. Yu, Z. Wen, G. Lu and J. Chen, Effects of N and F doping on structure and photocatalytic properties of anatase TiO_2 nanoparticles, *RSC Adv.*, 2013, **3**, 16657, DOI: 10.1039/C3RA42600A.

4 A. Pandikumar, K. Sivaranjani, C. S. Gopinath and R. Ramaraj, Aminosilicate sol–gel stabilized N-doped TiO_2–Au nanocomposite materials and their potential environmental remediation applications, *RSC Adv.*, 2013, **3**, 13390, DOI: 10.1039/C3RA40573G.

5 G. Pótári, D. Madarász, L. Nagy, B. László, A. Sápi, A. Oszkó, A. Kukovecz, A. Erdőhelyi, Z. Kónya and J. Kiss, Rh induced support transformation phenomena in titanate nanowire and nanotube catalysts, *Langmuir*, 2013, **29**, 3061–3072, DOI: 10.1021/la304470v.

6 W. Avansi Jr., R. Arenal, V. R. de Mendonça, C. Ribeiro and E. Longo, Vanadium-doped TiO_2 anatase nanostructures: the role of V in solid solution formation and its effect on the optical properties, *CrystEngComm*, 2014, **16**, 5021, DOI: 10.1039/C3CE42356E.

7 J. Xu, W. Wang, M. Shang, E. Gao, Z. Zhang and J. Ren, Electrospun nanofibers of Bi-doped TiO_2 with high photocatalytic activity under visible light irradiation, *J. Hazard. Mater.*, 2011, **196**, 426–430, DOI: 10.1016/j.jhazmat.2011.09.010.

8 H. Zhao, F. Tian, R. Wang and R. Chen, A review on Bismuth-related nanomaterials for photocatalysis, *Rev. Adv. Sci. Eng.*, 2014, **3**, 3, DOI: 10.1166/rase.2014.1050.

9 X. H. Xu, M. Wang, Y. Hou, W. F. Yao, D. Wang and H. Wang, Preparation and characterization of Bi-doped TiO_2 photocatalyst, *J. Mater. Sci. Lett.*, 2002, **21**, 1655–1656, DOI: 10.1023/A:1020800104179.

10 P. A. K. Reddy, B. Srinivas, P. Kala, V. D. Kumari and M. Subrahmanyam, Preparation and characterization of Bi-doped TiO_2 and its solar photocatalytic activity for the degradation of isoproturon herbicide, *Mater. Res. Bull.*, 2011, **46**, 1766–1771, DOI: 10.1016/j.materresbull.2011.08.006.

11 U. G. Akpan and B. H. Hameed, The advancements in sol-gel method of doped-TiO_2 photocatalysts, *Appl. Catal., A*, 2010, **375**, 1–11, DOI: 10.1016/j.apcata.2009.12.023.

12 T. Ji, F. Yang, Y. Lv, J. Zhou and J. Sun, Synthesis and visible-light photocatalytic activity of Bi-doped TiO_2 nanobelts, *Mater. Lett.*, 2009, **63**, 2044–2046, DOI: 10.1016/j.matlet.2009.06.043.

13 D. Dvoranová, V. Brezová, M. Mazúra and M. A. Malati, Investigations of metal-doped Titanium dioxide photocatalysts, *Appl. Catal., B*, 2002, **37**, 91–105, DOI: 10.1016/S0926-3373(01)00335-6.

14 D. A. Maslov, M. V. Tsodikov, S. A. Nikolaev, V. V. Kriventsov, V. A. Grinberg, V. V. Emets and N. A. Mayorova, Structural features and photoelectrocatalytic properties of Bismuth-doped Titanium oxides, *Mater. Chem. Phys.*, 2021, **259**, 123936, DOI: 10.1016/j.matchemphys.2020.123936.

15 N. Chakinala, P. Ratnakar Gogate and A. G. Chakinala, Highly efficient bi-metallic bismuth-silver doped TiO_2 photocatalyst for dye degradation, *Korean J. Chem. Eng.*, 2021, **38**(12), 2468–2478, DOI: 10.1007/s11814-021-0890-5.

16 Y. Iida and S. Ozaki, Grain growth and phase transformation of Titanium Oxide during calcinations, *J. Am. Ceram. Soc.*, 1961, **44**(3), 120–127, DOI: 10.1111/j.1151-2916.1961.tb13725.x.

17 R. Chauhan, A. Kumar and R. P. Chaudhary, Structural and photocatalytic studies of Mn doped TiO_2 nanoparticles, *Spectrochim. Acta, Part A*, 2012, **98**, 256–264, DOI: 10.1016/j.saa.2012.08.009.

18 M.-C. Wu, J.-S. Chih and W.-K. Huang, Bismuth doping effect on TiO_2 nanofibres for morphological change and photocatalytic performance, *CrystEngComm*, 2014, **16**, 10692–10699, DOI: 10.1039/C4CE01348D.

19 M. A. Gondal, T. A. Saleh and Q. Drmosh, Optical Properties of Bismuth Oxide Nanoparticles synthesized by pulsed laser ablation in liquids, *Sci. Adv. Mater.*, 2012, **4**, 507–510, DOI: 10.1166/sam.2012.1310.

20 L. Xu, L. Yang, E. M. J. Johansson, Y. Wang and P. Jin, Photocatalytic activity and mechanism of bisphenol a removal over TiO_{2-x}/rGO nanocomposite driven by visible light, *Chem. Eng. J.*, 2018, **350**, 1043–1055.

21 I. Altin, Bi-doped TiO_2 as a photocatalyst for enhanced photocatalytic activity, *Sakarya Univ. J. Sci.*, 2023, **27**, 670–679.

22 F. Moslehirad, M. H. Majles Ara, M. J. Torkamany, M. Afsary, M. Ghorannevis and J. Sabbaghzadeh, Thermal nonlinear optical properties of TiO_2 nanocrystals prepared through pulsed laser ablation, *Laser Phys.*, 2013, **23**, 055402, DOI: 10.1088/1054-660X/23/5/055402.

23 P. Makula, M. Pacia and W. Macyk, How to correctly determine the band gap energy of modified semiconductor based on UV-Vis spectra, *J. Phys. Chem. Lett.*, 2018, **9**, 6814–6817, DOI: 10.1021/acs.jpclett.8b02892.

24 L. Dong, H. Chu, Y. Li, S. Zhao and D. Li, Enhanced optical nonlinearity and ultrafast carrier dynamics of TiO_2/CuO nanocomposites, *Composites, Part B*, 2022, **237**, 109860, DOI: 10.1016/j.compositesb.2022.109860.

25 G. D. Bhowmick, Md. T. Noori, I. Das, B. Neethu, M. M. Ghangrekar and A. Mitra, Bismuth doped TiO_2 as an excellent photocathode catalyst to enhance the performance of microbial fuel cell, *Int. J. Hydrogen Energy*, 2018, **43**, 7501–7510, DOI: 10.1016/j.ijhydene.2018.02.188.

26 M. S. Bahae, A. A. Said, T. H. Wei, D. Hagan and E. W. V. Stryland, Sensitive measurement of optical nonlinearities using a single beam, *IEEE J. Quantum Electron.*, 1990, **26**, 760–769, DOI: 10.1109/3.53394.

27 R. A. Ganeev, A. I. Ryasnyansky, A. L. Stepanov and T. Usmanov, Saturated absorption and reverse saturated absorption of Cu:SuO_2 at $\lambda = 532$ nm, *Phys. Status Solidi B*, 2004, **241**, R1–R4, DOI: 10.1002/pssb.200309025.

28 R. A. Ganeev, R. I. Tugushev and T. Usmanov, Application of the Nonlinear Optical Properties of Platinum Nanoparticles for the Mode Locking of Nd: Glass Laser, *Appl. Phys. B*, 2009, **94**, 647–651, DOI: 10.1007/s00340-009-3371-9.

29 J. Twinkle, M. Suresh, B. Dipanjan and G. Krishna Podagatlapalli, Strong Two and Three-Photon Absorption Coefficients of Gold-Doped Titanium Di-Oxide Nanoparticles Achieved by Femtosecond Z-Scan Technique, *Plasmonics*, 2024, **19**, 2433–2447, DOI: 10.1007/s11468-023-02161-9.

30 J. Twinkle, S. Hamad, B. Dipanjan, M. Suresh and G. Krishna Podagatlapalli, Nonlinear optical studies of Bismuth-doped Titanium dioxide colloids achieved by femtosecond Z-Scan technique, *Opt. Mater.*, 2024, **15**, 116052, DOI: 10.1016/j.optmat.2024.116052.

31 L. G. Bousiakou, P. J. Dobson, T. Jurkin, I. Marić, O. Aldossary and M. Ivanda, Optical, structural and semiconducting properties of Mn doped TiO_2 nanoparticles for cosmetic applications, *J. King Saud Univ. Sci.*, 2022, **34**, 101818, DOI: 10.1016/j.jksus.2021.101818.

32 U. Caligulu, N. Darcan and H. Kejanli, Surface morphology and optical properties of Ca and Mn doped TiO_2 nanostructured thin films, *Eng. Sci. Technol. Int. J.*, 2021, **24**, 1292–1300, DOI: 10.1016/j.jestch.2021.05.006.

33 D. Banerjee, S. S. B. Moram, C. Byram, J. Rathod, T. Jena, G. Krishna Podagatlapalli and S. V. Rao, Plasmon-enhanced ultrafast and tunable thermo-optic nonlinear optical properties of femtosecond laser ablated TiO_2 and Silver-doped TiO_2 nanoparticles, *Appl. Surf. Sci.*, 2021, **569**, 151070, DOI: 10.1016/j.apsusc.2021.151070.

34 M. Falconieri, Thermo-optical effects in Z-scan measurements using high-repetition-rate lasers, *J. Opt. A: Pure Appl. Opt.*, 1999, **1**, 662, DOI: 10.1088/1464-4258/1/6/302.

35 A. J. Twarowski and D. S. Kliger, Multiphoton absorption spectra using thermal blooming, *Chem. Phys.*, 1977, **20**, 253–258, DOI: 10.1016/0301-0104(77)85029-5.

36 J. Lin, Y. Chen, H. Lin and W. Hsieh, Two-photon resonance assisted huge nonlinear refraction and absorption in ZnO thin films, *J. Appl. Phys.*, 2005, **97**, 033526, DOI: 10.1063/1.1848192.

37 A. Rambabu, S. Sheetal, S. Akanksha, Y. Balaji, S. V. Rao, S. Hamad and G. Krishna Podagatlapalli, Strong two-photon absorption and reduced thermal effects in aluminum and silver-doped Pt nanoparticles, *Opt. Laser Technol.*, 2023, **160**, 109032, DOI: 10.1016/j.optlastec.2022.109032.